Constraints on nonstandard intermediate boson exchange models from neutrino-electron scattering

B. Sevda,[1,2] A. Şen,[1] M. Demirci,[3] M. Deniz,[1,2,*] M. Agartioglu,[1,2] A. Ajjaq,[1] S. Kerman,[1,2] L. Singh,[2,4] A. Sonay,[1,2] H. T. Wong,[2] and M. Zeyrek[5]

[1]*Department of Physics, Dokuz Eylül University, Buca, İzmir TR35160, Turkey*
[2]*Institute of Physics, Academia Sinica, Taipei 115, Taiwan*
[3]*Department of Physics, Karadeniz Technical University, Trabzon TR61080, Turkey*
[4]*Department of Physics, Banaras Hindu University, Varanasi 221005, India*
[5]*Department of Physics, Middle East Technical University, Ankara TR06800, Turkey*

(Received 9 February 2017; published 21 August 2017)

Constraints on couplings of several beyond-Standard-Model-physics scenarios, mediated by massive intermediate particles including (1) an extra Z-prime, (2) a new light spin-1 boson, and (3) a charged Higgs boson, are placed via the neutrino-electron scattering channel to test the Standard Model at a low energy-momentum transfer regime. Data on $\bar{\nu}_e - e$ and $\nu_e - e$ scattering from the TEXONO and LSND, respectively, are used. Upper bounds to coupling constants of the flavor-conserving and flavor-violating new light spin-1 boson and the charged Higgs boson with respect to different mediator masses are determined. The relevant parameter spaces are extended by allowing light mediators. New lower mass limits for extra Z-prime gauge boson models are also placed.

DOI: 10.1103/PhysRevD.96.035017

I. INTRODUCTION

Recent discovery of nonzero neutrino mass and mixing undoubtedly implies new physics beyond the Standard Model (BSM). Nevertheless, the origin of the masses of neutrinos and absolute mass scale remain unknown. The seesaw mechanisms, R-parity-violating supersymmetry (SUSY), TeV scale loop mechanisms, extra dimensions, and string theory are the most popular proposals attempting to answer these questions and explain the origin of neutrino mass [1]. However, in the underlying new physics BSM, it is mostly expected that the structure of electroweak charged and neutral currents of the Standard Model (SM) would also change. Such changes in the neutrino sector lead to nonstandard interactions (NSI) of neutrinos. In many works on NSI, new interactions are generally mediated by new particles, which are assumed to be heavier than the electroweak scale. Hence, these are carried out in the form of effective four-fermion interaction at low energy. Furthermore, it is also possible mediated new particles can have relatively low masses.

Neutrino interactions, being pure leptonic processes, are one of the most appropriate mechanisms to test the electroweak theory of the SM [2–5]. Therefore, the $\nu_e(\bar{\nu}_e) - e$ elastic scattering can be used to search for BSM new physics scenarios mediated by a massive intermediate boson such as the extra Z-prime gauge boson (Z'), new light spin-1 boson (NLS1B), and charged Higgs boson (CHB), which are predicted by certain models to describe new interactions mediated by new particles in addition to the SM electroweak Z and W gauge bosons.

In this paper, we report experimental constraints on the masses and coupling parameters for the exchange of the NLS1B and CHB as well as lower mass limits on Z' from $\nu_e - e$ and $\bar{\nu}_e - e$ elastic scattering.

II. NEUTRINO-ELECTRON SCATTERING AND DATA

A. Standard Model

Since incoming neutrinos are of electron-type flavor, $\nu_e(\bar{\nu}_e) - e$ elastic scattering can occur via both charged current and neutral current interaction. Therefore, their interference, which is destructive, also contributes to the cross section. The SM differential cross section of $\nu_e(\bar{\nu}_e) - e$ elastic scattering can be expressed in the laboratory frame as [6–10]

$$\left[\frac{d\sigma}{dT}\left(\overset{(-)}{\nu}_e e\right)\right]_{\mathrm{SM}} = \frac{2G_F^2 m_e}{\pi}\left[a^2 + b^2\left(1 - \frac{T}{E_\nu}\right)^2 - ab\frac{m_e T}{E_\nu^2}\right], \tag{1}$$

where G_F is the Fermi coupling constant, T is the kinetic energy of the recoil electron, E_ν is the incident neutrino energy, and the coefficients of a and b are given in Table I in terms of chiral coupling constants g_R and g_L, weak mixing angle $\sin^2\theta_W$, and vector–axial-vector coupling constants g_V and g_A, which are defined as $-1/2 + 2\sin^2\theta_W$ and $-1/2$, respectively.

*muhammed.deniz@deu.edu.tr

TABLE I. Coefficients in the expression of the SM differential cross section of $\bar{\nu}_e - e$ and $\nu_e - e$ scattering given in Eq. (1).

Coefficients	$\bar{\nu}_e - e$	$\nu_e - e$
	$(g_V - g_A)/2$	$(g_V + g_A + 2)/2$
a	$\sin^2\theta_W$	$\sin^2\theta_W + 1/2$
	g_R	$g_L + 1$
	$(g_V + g_A + 2)/2$	$(g_V - g_A)/2$
b	$\sin^2\theta_W + 1/2$	$\sin^2\theta_W$
	$g_L + 1$	g_R

B. Input data

The analysis of the experimental data sets of TEXONO, as a sample of the antineutrino channel at low energy with three different detectors located at KSNL whose energy ranges are different, and LSND, as a sample of the neutrino channel at high energy, is reported. The published results of the differential cross section measurements are used for each sample. The results from three independent data sets of the TEXONO $\bar{\nu}_e - e$ interaction are compared with those from the LSND $\nu_e - e$ interaction.

TEXONO Experiment: Three experimental data sets taken with different detectors are used as follows:

CsI(Tl): 29882/7369 kg-days of reactor on/off data: $\bar{\nu}_e - e^-$ electroweak interaction cross section, g_V, g_A, weak mixing angle $\sin^2\theta_W$, and charge radius squared were measured with an effective mass of 187 kg CsI(Tl) crystal scintillator array at 3–8 MeV_{ee}. The root-mean-square (RMS) energy resolutions are 5.8%, 5.2%, and 4.0% at ^{137}Cs, ^{40}K, and ^{208}Tl γ peaks, respectively. The residual reactor on—reactor off event rate spectrum at 3–8 MeV_{ee} shown in Fig. 16(b) of Ref. [11] is used for this analysis.

HP-Ge: 570.7/127.8 kg-days of reactor on/off data: New limits are set to the neutrino magnetic moment and axion with a target mass of 1.06 kg high-purity germanium detector [12] at 12–64 keV_{ee}. The RMS energy resolution of HP-Ge is 880 keV_{ee} at Ga-K shell x-ray energy [13]. The residual reactor on—reactor off event rate spectrum at 12–64 keV_{ee} shown in Fig. 13 of Ref. [12] is used for this analysis.

PC-Ge: 124.2/70.3 kg-days of reactor on/off data: New limits are set to neutrino millicharge and low mass weakly interacting massive particle (WIMP) with a fiducial mass of 500 g point contact germanium (PC-Ge) detector [8] at the 0.3–12 keV_{ee} energy region. The RMS energy resolution of PC-Ge is 87 keV_{ee} at Ga-K shell x-ray energy [13]. The residual reactor on—reactor off event rate spectrum at 0.3–12 keV_{ee} shown in Fig. 4 of Ref. [8] is used for this analysis.

LSND Experiment: The Liquid Scintillator Detector at the Los Alamos Neutron Science Center was exposed to electron neutrinos produced at the proton beam stop with electron recoil energy T of 18–50 MeV_{ee}. The cross section for the elastic scattering reaction $\nu_e - e$ and weak mixing angle $\sin^2\theta_W$ were measured. The energy resolution was determined from the shape of the electron energy spectrum and was found to be 6.6% at the 52.8 MeV end point. The observed and expected distribution of beam-excess events at 18–50 MeV_{ee} published in Fig. 10 of Ref. [14] are adopted in this analysis.

LAMPF ν_e − e Experiment: A 15 ton fine-grained tracking calorimeter surrounded by multiwire proportional chambers (MWPCs) was exposed to electron neutrinos from muon decay at rest with T of 7–60 MeV_{ee} at the Los Alamos Meson Physics Facility, now renamed the Los Alamos Neutron Science Center. In this experiment, neutrino-electron elastic scattering was observed and electroweak parameters were measured. From the agreement between the measured and SM expectation, limits on neutrino properties (such as neutrino flavor changing neutral currents and neutrino electromagnetic moments) and limits on the masses of new bosons [such as neutral tensor and pseudo(scalar) boson, charged Higgs boson, and a purely left-handed charged (neutral) vector boson] were derived in Ref. [15].

C. Analysis methods

The expected event rate of R can be calculated as

$$R_X = \rho_e \int_T \int_{E_\nu} \left[\frac{d\sigma}{dT}\right]'_X \frac{d\phi(\bar{\nu}_e)}{dE_\nu} dE_\nu dT, \tag{2}$$

where ρ_e is the electron number density per kg of target mass, and $d\phi/dE_\nu$ is the neutrino spectrum. X represents different interaction channels such as SM, NLS1B, CHB, etc.

The measurable differential cross section is denoted by $[d\sigma/dT]'$ and corresponds to a convolution of the detector energy resolution to the physical differential cross section $[d\sigma/dT]$. In practice, as far as BSM scenarios and experimental data studied in this work are concerned, the variations of $[d\sigma/dT]$ with energy are gradual, so that the resolution smearing does not significantly alter the measured spectra in the region of interest. The difference between $[d\sigma/dT]$ and $[d\sigma/dT]'$ is less than 0.1%. Accordingly, resolution effects can be neglected in this analysis. R_{expt} is expressed in units of kg^{-1} MeV^{-1} day^{-1} and kg^{-1} keV^{-1} day^{-1} for the CsI(Tl) and Ge data sets, respectively.

The published neutrino spectra for ν_e, ν_μ, $\bar{\nu}_\mu$ [14] are used to derive the SM differential cross sections for the LSND analysis. The number of measured physical and background events are taken from Fig. 10 and Table III of Ref. [14]. The published total cross section measured values are used for normalization:

$$\sigma_{\text{expt}} = [10.1 \pm 1.1(\text{stat}) \pm 1.0(\text{sys})] \times E_{\nu_e} \times 10^{-45}\ \text{cm}^2$$
$$\sigma_{\text{SM}} = 9.3 \times E_{\nu_e} \times 10^{-45}\ \text{cm}^2. \tag{3}$$

The results on physics couplings from this analysis are expressed either as "best-fit ± statistical ± systematic uncertainties" at the 1σ level, or in terms of limits at a 90% or 95% confidence level (C.L.). The statistical uncertainties are derived by the minimum χ^2 method, defined as

$$\chi^2 = \sum_{i=1} \left[\frac{R_{\rm expt}(i) - R_{\rm SM}(i) - R_X(i)}{\Delta(i)} \right]^2, \qquad (4)$$

where $R_{\rm expt}$ is the measured rate; and $R_{\rm SM}$ and R_X are the expected event rates for SM and X (with $X = Z'$, NLS1B, CHB, etc.), respectively; and $\Delta(i)$ is the ith bin statistical uncertainty published by the experiments. The published systematic uncertainties of the experiments contribute to shifts of the best-fit values in the physics couplings. The two contributions are added in quadrature to give rise to the combined uncertainties, from which the 90% or 95% C.L. limits can be derived using the prescription of Ref. [16].

III. INTERMEDIATE BOSONS BEYOND THE STANDARD MODEL

Some of the BSM involve exchanging of massive intermediate bosons such as the extra Z', NLS1B, and CHB in addition to the SM Z and W gauge bosons. A Feynman diagram of neutrino and antineutrino scattering off electron for various NSI scenarios is illustrated in Fig. 1.

Some of the new physics BSMs have a mechanism giving mass to neutrinos such as low-energy SUSY with R-parity breaking, an extra Higgs boson, unified SUSY models, etc. Indeed, any BSM physics model should reproduce current data and therefore should include massive neutrinos. In addition, there are some recent model-dependent BSM studies in the literature [17,18]. In this paper, we only study some specific models for new interactions with massive virtual bosons. In the following sections these BSM scenarios and their corresponding experimental constraints will be discussed in detail.

NSI can simply be considered as modifications of coupling constants with additional new terms in the chiral couplings of $g_{R,L}$ in general. Therefore, for the flavor-conserving (FC) NSI cases, the new couplings can be expressed as

$$g_{R(L)} \to \tilde{g}_{R(L)} = g_{R(L)} + \tilde{\varepsilon}_{ee}^{R(L)}. \qquad (5)$$

The $\bar{\nu}_{\rm e} - {\rm e}$ and $\nu_{\rm e} - {\rm e}$ scattering differential cross sections can be written in terms of new couplings of FC and flavor-violating (FV) NSI of neutrinos given in Table II. The differential cross section of BSM contributions can be obtained by using Eq. (1) together with the coefficients

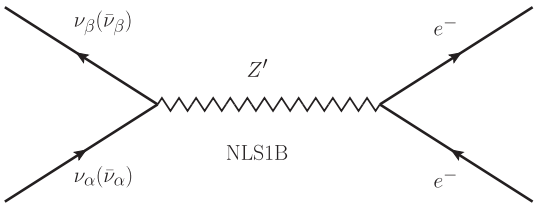

FIG. 1. Feynman diagram for $\nu_{\rm e}(\bar{\nu}_{\rm e}) - e$ via exchange of massive mediators such as the virtual Z' or NLS1B.

TABLE II. Coefficients with BSM contributions in expressions of the differential cross section of $\nu_{\rm e}(\bar{\nu}_{\rm e}) - e$ scattering given in Eq. (1).

Coefficients	$\bar{\nu}_e - e$	$\nu_e - e$
a^2	$\tilde{g}_R^2 + \sum_{\ell' \neq e} \lvert\tilde{\varepsilon}_{e\ell'}^R\rvert^2$	$(\tilde{g}_L + 1)^2 + \sum_{\ell' \neq e} (\tilde{\varepsilon}_{e\ell'}^L)^2$
b^2	$(\tilde{g}_L + 1)^2 + \sum_{\ell' \neq e} \lvert\tilde{\varepsilon}_{e\ell'}^L\rvert^2$	$\tilde{g}_R^2 + \sum_{\ell' \neq e} (\tilde{\varepsilon}_{e\ell'}^R)^2$
ab	$\tilde{g}_R(\tilde{g}_L + 1) + \sum_{\ell' \neq e} \lvert\tilde{\varepsilon}_{e\ell'}^R\rvert\lvert\tilde{\varepsilon}_{e\ell'}^L\rvert$	

from Table II considering both FC NSI and FV NSI with $\ell' = \mu$ or τ.

A. Extra Z' gauge boson

Intermediate particles of electroweak interaction, in addition to SM $W^{\pm}$ and Z^0 gauge bosons, have engaged particle physicists' attention for a long while since they are a common feature of many models aiming to define the nature of BSM. The Z' gauge boson, the new gauge boson, was proposed as a theoretical particle resulting from the expansion of electroweak interactions in particle physics. Its name comes from the SM Z boson.

New massive U(1) gauge bosons emerge in grand unified and superstring theories such as SO(10) and E_6 [19], in theories of extra space-time dimensions of the SM gauge bosons [20]. In this study, we will not restrict ourselves to SM gauge bosons. In fact, we will consider a possible new vector boson predicted in many extensions of the SM called the Z' gauge boson, which is a massive, electrically neutral and color-singlet hypothetical particle of spin 1.

There are various physical models of BSM that suggest different Z' bosons. The most popular of them are the E_6-string-type model, left-right symmetric model, and the sequential Standard Model (SSM). The E_6-string-type model, based on E_6 symmetries, contains the $SO(10) \times U(1)_\psi$ and $SU(5) \times U(1)_\chi$, which means that the two Z' states (i.e., Z'_χ and Z'_ψ) are included and can mix by some angle β. The mixing of these two states is given by their linear combination as $Z'(\beta) = Z'_\chi(\cos\beta) + Z'_\psi(\sin\beta)$ [21].

The new coupling parameters of BSM are generally obtained by modifying the ordinary coupling constants of the SM. Therefore, the new cross sections for the interactions via the exchange of an extra Z' gauge boson can be obtained by replacing the SM couplings appearing in Eq. (1) with the new modified couplings accordingly.

The new differential cross section of Z' models for $\nu_e(\bar{\nu}_e) - e$ elastic scattering can be obtained by modifying the couplings with

$$\tilde{\varepsilon}_{ee}^R = 2\gamma \sin^2\theta_W \rho_{\nu e}^{NC} \left(\frac{c_\beta}{2\sqrt{6}} - \frac{s_\beta}{3}\sqrt{\frac{5}{8}} \right) \left(\frac{3c_\beta}{2\sqrt{6}} + \frac{s_\beta}{3}\sqrt{\frac{5}{8}} \right)$$

$$\tilde{\varepsilon}_{ee}^L = 2\gamma \sin^2\theta_W \rho_{\nu e}^{NC} \left(\frac{3c_\beta}{2\sqrt{6}} + \frac{s_\beta}{3}\sqrt{\frac{5}{8}} \right)^2, \qquad (6)$$

where $c_\beta = \cos\beta$, $s_\beta = \sin\beta$, and $\gamma = (M_Z/M_{Z'})^2$.

In this paper, three main models of the E_6-string-type model [22] have been investigated: the χ model where $\cos\beta = 1$, the ψ model where $\cos\beta = 0$, and the η model where $\cos\beta = \sqrt{3/8}$.

One of the other popular models proposing a heavy neutral vector boson is the left-right symmetric model, which has breaking dynamical symmetry. The left-right symmetric model is based on $SU(2)_L \times SU(2)_R \times U(1)_{B-L}$, where $SU(2)_L$ and $SU(2)_R$ are associated to the left-handed and right-handed weak isospins, respectively, and $U(1)_{BL}$ is associated to the charge $Q_{BL} = B - L$, where B and L are the baryon and lepton number, respectively. The couplings are constructed in this model as

$$\tilde{g}_R = Ag_R + Bg_L \quad \text{and}$$
$$\tilde{g}_L = Ag_L + Bg_R, \tag{7}$$

where the parameters of A and B can be described as

$$A = 1 + \frac{\sin^4\theta_W}{1 - 2\sin^2\theta_W}\gamma \quad \text{and}$$
$$B = \frac{\sin^2\theta_W(1 - \sin^2\theta_W)}{1 - 2\sin^2\theta_W}. \tag{8}$$

Finally, the SSM, Z'_{SSM}, is defined as having the same couplings with quarks and leptons, which are identical to those of the SM Z, and decays of only known fermions. This model serves as a useful reference case when comparing the Z' researches with well-motivated models [21]. The differential cross section for this model can be written as

$$\left[\frac{d\sigma}{dT}(\bar{\nu}_e e)\right]_{Z'_{\mathrm{SSM}}} = \frac{2G_F^2 m_e}{\pi}\left\{\gamma\left[4g_L\left(1 - \frac{T}{E_\nu}\right)^2 - 2g_R\frac{m_e T}{E_\nu^2}\right] + \gamma^2\left[g_R^2 + g_L^2\left(1 - \frac{T}{E_\nu}\right)^2 - g_R g_L\frac{m_e T}{E_\nu^2}\right]\right\}. \tag{9}$$

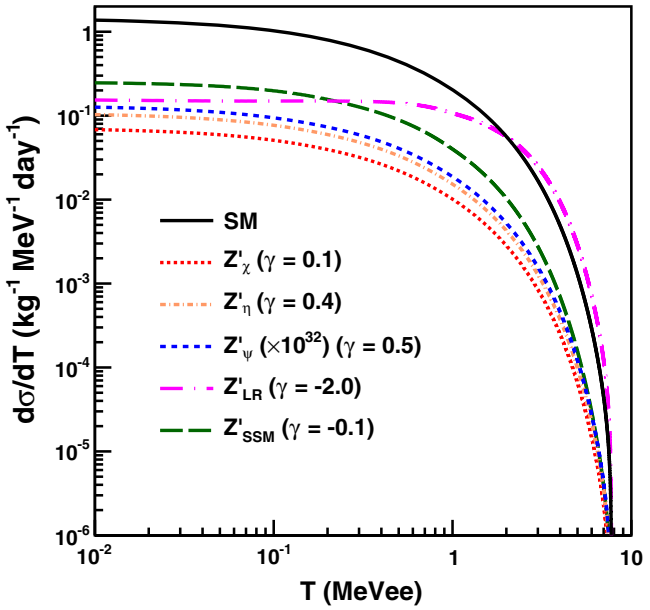

FIG. 2. Differential cross section as a function of the recoil energy T with typical reactor $\bar{\nu}_e$ spectra for extra Z' models for a specific γ value using CsI(Tl) as a target, where $\gamma = (M_Z/M_{Z'})^2$. The SM contributions are superimposed for comparison.

The differential cross sections for various extra Z' models with the use of CsI(Tl) as a target at a specific value of γ are displayed in Fig. 2, where the SM contribution is superimposed for comparison. As it can be seen in the figure, the cross sections of different Z' models demonstrate similar behavior with respect to the recoil energy of the electron. Working at the MeV-energy regime has many more advantages than working at low energy since the cross sections of the SM were measured more precisely with CsI(Tl) data. Therefore, more stringent limits are set to the mass of the extra Z' gauge boson with the CsI(Tl) detector data set compared to those of Ge detector data sets.

By adopting a minimum χ^2 analysis, the best-fit results and the lower bounds for the mass of the Z' gauge boson obtained from the CsI(Tl) detector data set for each Z' model are given in Table III. The projected sensitivities and the present bounds from the LHC experiment are also given for comparison. It can be seen that the bounds from low-energy

TABLE III. Constraints on $M_{Z'}$ at 95% C.L. obtained from the best fit on γ, current limits, and projected sensitivities on $M_{Z'}$ bounds by improving 1% in the accuracies of CsI(Tl) data.

Model		Best fit for γ (1σ)	χ^2_{min}/dof	$M_{Z'}$ bounds at 95% C.L. (GeV)	Projected (1%) $M_{Z'}$ bounds at 95% C.L. (GeV)	Current limit [PDG 2016] at 95% C.L. (GeV)
E_6 string type	Z'_χ	$0.16 \pm 0.41 \pm 0.31$	8.7/9	>85	>915	>1970 (ATLAS)
	Z'_η	$0.43 \pm 1.01 \pm 0.83$	8.7/9	>52	>566	>1870 (ATLAS)
	Z'_ψ	$[0.44 \pm 1.13 \pm 0.95] \times 10^{-18}$	8.7/9	>0	>0	>2260 (CMS)
Z'_{LR}		$-8.02 \pm 5.28 \pm 0.61$	7.8/9	>44	>413	>1162 (RVUE)
Z'_{SSM}		$-0.04 \pm 0.14 \pm 0.06$	8.7/9	>172	>1822	>1830 (ATLAS)

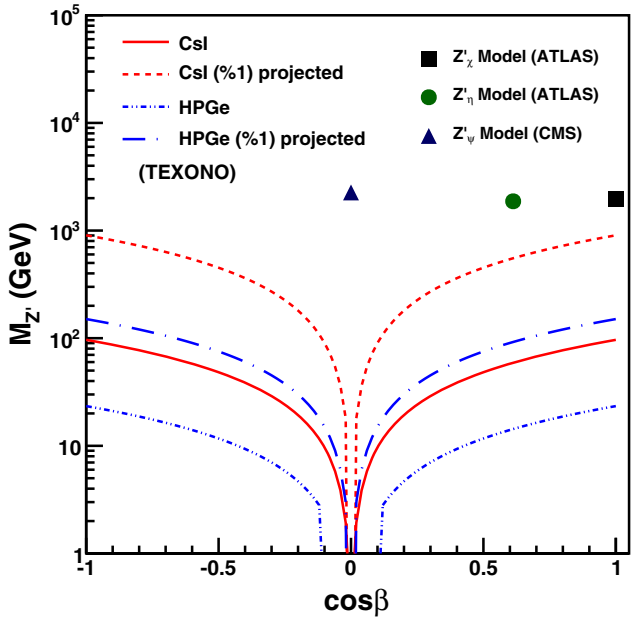

FIG. 3. The lower limit for the mass of Z' at 95% C.L. using the TEXONO CsI(Tl) and HP-Ge detector data sets for the mixing-parameter-independent case of the E6-string-type model. Projected sensitivities by improving the experimental accuracies to 1% are superimposed.

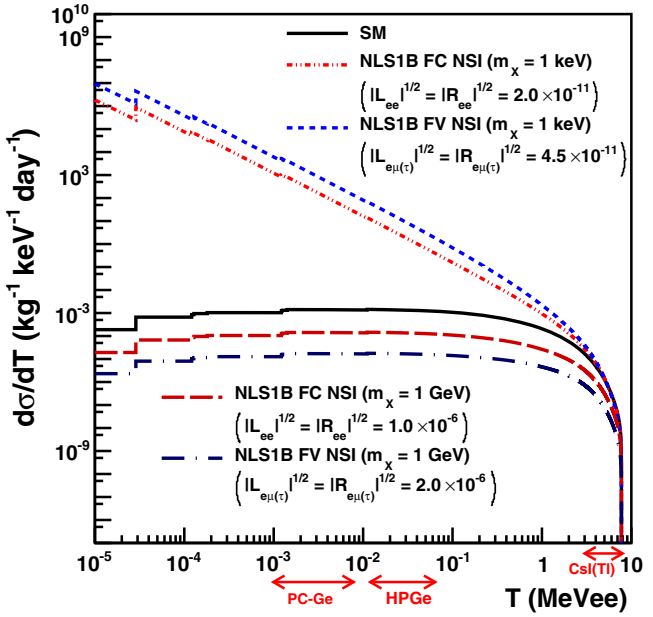

FIG. 4. Differential cross section as a function of the recoil energy T with typical reactor $\bar{\nu}_e$ spectra for the NLS1B at some specific coupling and mass parameters relevant to this work using Ge as a target for both the FC and FV cases. The SM contributions are superimposed for comparison.

neutrino-electron scattering experiments are much less stringent than those of high-energy collider experiments, due to worse statistics and in general a larger background.

The realistic sensitivities of future reactor $\bar{\nu}_e - e$ scattering experiments are discussed in Table VII of Ref. [11]. The main improvement is due to background suppression. The effects of a projected accuracy of 1% to the various $M_{Z'}$ bounds are also shown in Table III. The aim of this extrapolation is to see how the Z' mass bounds are related to the experimental accuracies. It may provide intuitive scaling for the future neutrino experiments. Moreover, the mixing-parameter-independent sensitivities of CsI(Tl) and HP-Ge detector data at 95% C.L. for E_6-string-type Z' models are shown in Fig. 3. It can be seen from the figure that the χ model, where $\cos\beta = 1$, can provide a more stringent limit.

B. New light spin-1 boson

The exchange of new massive particles can be a possible origin of NSI of neutrinos, manifested as anomalies in the measurable total or differential cross sections. These massive particles, however, can be as light as in the order of a few MeV scale, which is the range of low-energy experiments. The NLS1B is one of the examples of such kinds of particles. A spin-1 particle could also be involved in explaining the NuTeV anomaly [23]. In addition to this, the NLS1B may also explain the muon anomalous magnetic moment value [24]. Moreover, spin-1 bosons can couple to dark matter and the nonbaryonic matter of the Universe in the MeV scale region. They could be responsible for the annihilation that is seen as the unexplained 511 keV gamma emissions anomaly from the galactic bulge [25]. Furthermore, the NLS1B particle, which is lighter than b quarks, would explain the anomalous CP-violation in the mixing of neutral B-mesons. [26]. The effective Lagrangian for the NLS1B can be written as [27]

$$\mathcal{L}_X = -g_{\nu_\ell\nu_{\ell'}}\bar{\nu}_\ell\gamma^\mu P_L\nu_{\ell'}X_\mu - \bar{e}\gamma^\mu(L_{e\ell'}P_L + R_{e\ell'}P_R)eX_\mu, \tag{10}$$

where $P_{R,L} = (1 \pm \gamma^5)/2$ are the chiral projectors and the labels ℓ, ℓ' correspond to lepton flavor e, μ, or τ.

The $\nu_e(\bar{\nu}_e) - e$ scattering differential cross section for NLS1B exchange contributions can be obtained by modifying the chiral couplings as given in Table II. The $\tilde{\varepsilon}^{R(L)}_{e\ell'}$ can be defined in terms of the coupling parameters $R_{e\ell'}, L_{e\ell'}$, and the mass of m_X as

$$\tilde{\varepsilon}^R_{e\ell'} = \frac{R_{e\ell'}}{2\sqrt{2}G_F(2m_eT + m_X^2)} = \frac{m_X^2}{2m_eT + m_X^2}\varepsilon^R_{e\ell'}$$
$$\tilde{\varepsilon}^L_{e\ell'} = \frac{L_{e\ell'}}{2\sqrt{2}G_F(2m_eT + m_X^2)} = \frac{m_X^2}{2m_eT + m_X^2}\varepsilon^L_{e\ell'}, \tag{11}$$

where $\ell' = e$, μ, or τ, and $\varepsilon^{R(L)}_{e\ell'}$ can be defined as

$$\varepsilon^R_{e\ell'} = \frac{R_{e\ell'}}{2\sqrt{2}G_Fm_X^2} \quad \varepsilon^L_{e\ell'} = \frac{L_{e\ell'}}{2\sqrt{2}G_Fm_X^2}. \tag{12}$$

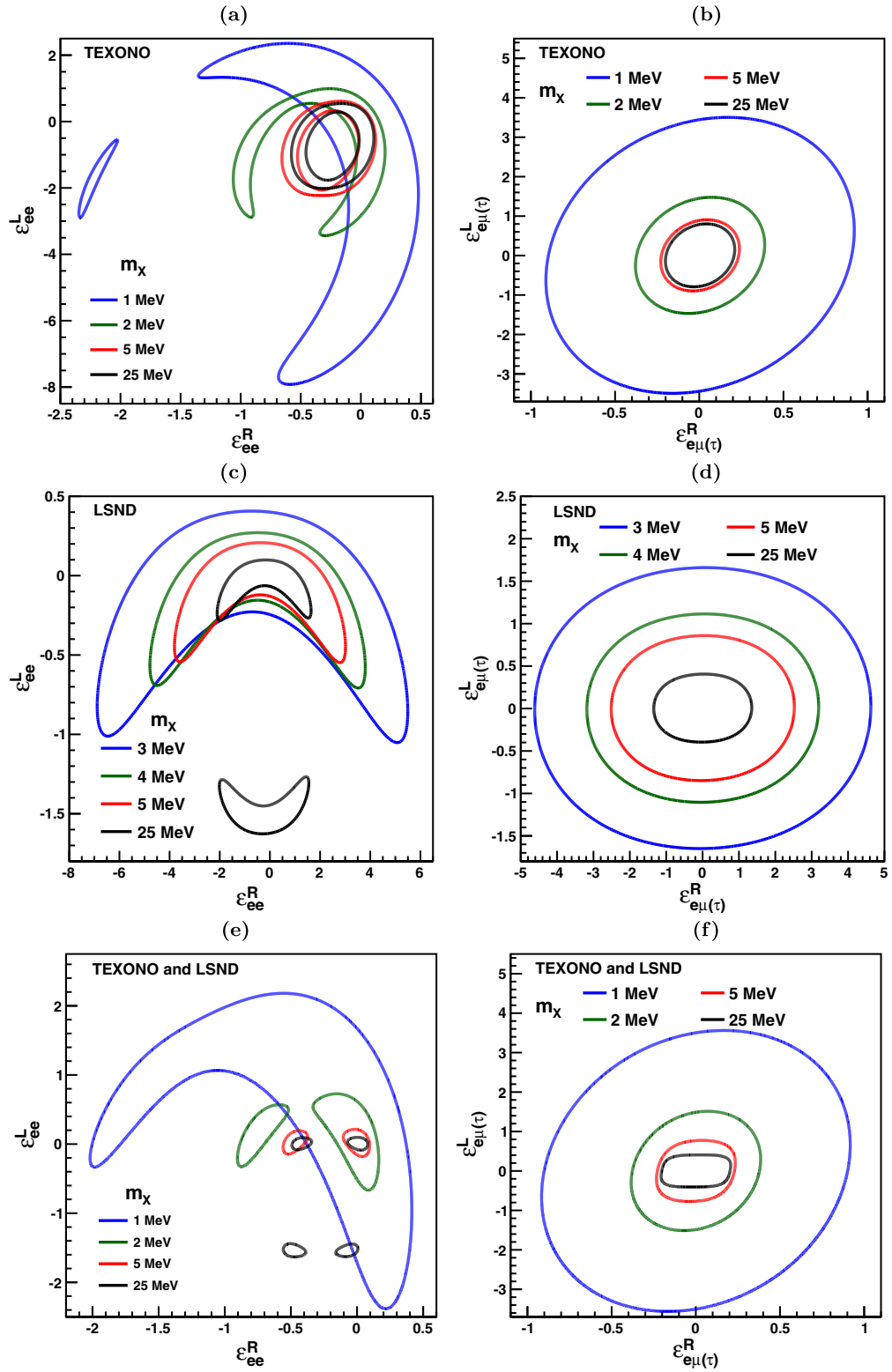

FIG. 5. The allowed regions at 90% C.L. for (a) the FC NLS1B in the parameter space of ε^L_{ee} and ε^R_{ee}; (b) FV NLS1B in the parameter space of $\varepsilon^L_{e\mu(\tau)}$ and $\varepsilon^R_{e\mu(\tau)}$ for TEXONO CsI(Tl) with various $m_X = 1, 2, 5, 25$ MeV, from outer to inner, respectively; (c) FC NLS1B in the parameter space of ε^L_{ee} and ε^R_{ee}; (d) FV NLS1B in the parameter space of $\varepsilon^L_{e\mu(\tau)}$ and $\varepsilon^R_{e\mu(\tau)}$ for LSND with various $m_X = 3, 4, 5, 25$ MeV, from outer to inner, respectively, with the global fitting for allowed regions of TEXONO CsI(Tl) and LSND at 90% C.L. for (e) FC NLS1B couplings of ε^L_{ee} vs ε^R_{ee} and (f) FV NLS1B couplings of $\varepsilon^L_{e\mu(\tau)}$ vs $\varepsilon^R_{e\mu(\tau)}$ with various $m_X = 1, 2, 5, 25$ MeV from outer to inner, respectively.

TABLE IV. Constraints at 90% C.L. on the couplings for the FC NLS1B with $m_X^2 \ll 2m_eT$ and $m_X^2 \gg 2m_eT$ for the TEXONO and LSND data sets obtained from a one-parameter-at-a-time analysis.

$(m_X^2 \ll 2m_eT)$		$(m_X^2 \gg 2m_eT)$	
TEXONO PC-Ge $(\times 10^{-6})$	LSND $(\times 10^{-6})$	TEXONO CsI(Tl) $(\times 10^{-6})$	LSND $(\times 10^{-6})$
$\lvert L_{ee}\rvert^{1/2} < 1.21$	$\lvert L_{ee}\rvert^{1/2} < 10.12$	$\lvert L_{ee}\rvert^{1/2}/m_X < 2.58$	$\lvert L_{ee}\rvert^{1/2}/m_X < 1.87$
$\lvert R_{ee}\rvert^{1/2} < 1.22$	$\lvert R_{ee}\rvert^{1/2} < 31.42$	$\lvert R_{ee}\rvert^{1/2}/m_X < 1.87$	$\lvert R_{ee}\rvert^{1/2}/m_X < 8.63$
$\lvert V_{ee}\rvert^{1/2} < 1.02$	$\lvert V_{ee}\rvert^{1/2} < 9.95$	$\lvert V_{ee}\rvert^{1/2}/m_X < 1.58$	$\lvert V_{ee}\rvert^{1/2}/m_X < 1.84$
$\lvert A_{ee}\rvert^{1/2} < 1.02$	$\lvert A_{ee}\rvert^{1/2} < 10.22$	$\lvert A_{ee}\rvert^{1/2}/m_X < 1.33$	$\lvert A_{ee}\rvert^{1/2}/m_X < 1.88$

TABLE V. Constraints at 90% C.L. on the couplings for the FV NLS1B with $m_X^2 \ll 2m_eT$ and $m_X^2 \gg 2m_eT$ for the TEXONO and LSND data sets obtained from a one-parameter-at-a-time analysis.

$(m_X^2 \ll 2m_eT)$		$(m_X^2 \gg 2m_eT)$	
TEXONO PC-Ge $(\times 10^{-6})$	LSND $(\times 10^{-6})$	TEXONO CsI(Tl) $(\times 10^{-6})$	LSND $(\times 10^{-6})$
$\lvert L_{e\mu(\tau)}\rvert^{1/2} < 0.94$	$\lvert L_{e\mu(\tau)}\rvert^{1/2} < 19.15$	$\lvert L_{e\mu(\tau)}\rvert^{1/2}/m_X < 5.16$	$\lvert L_{e\mu(\tau)}\rvert^{1/2}/m_X < 3.63$
$\lvert R_{e\mu(\tau)}\rvert^{1/2} < 0.94$	$\lvert R_{e\mu(\tau)}\rvert^{1/2} < 30.75$	$\lvert R_{e\mu(\tau)}\rvert^{1/2}/m_X < 2.57$	$\lvert R_{e\mu(\tau)}\rvert^{1/2}/m_X < 6.48$
$\lvert V_{e\mu(\tau)}\rvert^{1/2} < 0.79$	$\lvert V_{e\mu(\tau)}\rvert^{1/2} < 18.58$	$\lvert V_{e\mu(\tau)}\rvert^{1/2}/m_X < 2.59$	$\lvert V_{e\mu(\tau)}\rvert^{1/2}/m_X < 3.56$
$\lvert A_{e\mu(\tau)}\rvert^{1/2} < 0.79$	$\lvert A_{e\mu(\tau)}\rvert^{1/2} < 18.50$	$\lvert A_{e\mu(\tau)}\rvert^{1/2}/m_X < 2.48$	$\lvert A_{e\mu(\tau)}\rvert^{1/2}/m_X < 3.55$

We can alternatively define new couplings $V(A)_{e\ell'}$ and $\tilde{\varepsilon}^{V(A)}_{e\ell'}$ similar to the SM chiral couplings of g_L, g_R in the case of one of the couplings not being zero as

$$\begin{aligned} V_{e\ell'} &= (L_{e\ell'} + R_{e\ell'})/2 \\ A_{e\ell'} &= (L_{e\ell'} - R_{e\ell'})/2 \\ \tilde{\varepsilon}^{V(A)}_{e\ell'} &= \frac{\tilde{\varepsilon}^{L}_{e\ell'} \pm \tilde{\varepsilon}^{R}_{e\ell'}}{2} = \frac{m_X^2}{2m_eT + m_X^2}\frac{\varepsilon^{L}_{e\ell'} \pm \varepsilon^{R}_{e\ell'}}{2} \\ &= \frac{m_X^2}{2m_eT + m_X^2}\varepsilon^{V(A)}_{e\ell'}, \end{aligned} \tag{13}$$

where $\varepsilon^{V(A)}_{e\ell'}$ can be defined as

$$\begin{aligned} \varepsilon^{V}_{e\ell'} &= \frac{\varepsilon^{L}_{e\ell'} + \varepsilon^{R}_{e\ell'}}{2} = \frac{V_{e\ell'}}{2\sqrt{2}G_F m_X^2} \\ \varepsilon^{A}_{e\ell'} &= \frac{\varepsilon^{L}_{e\ell'} - \varepsilon^{R}_{e\ell'}}{2} = \frac{A_{e\ell'}}{2\sqrt{2}G_F m_X^2}. \end{aligned} \tag{14}$$

TABLE VI. Upper bounds at 90% C.L. on the coupling of h_{ee} in CHB interaction for $\bar{\nu}_e - e$ and $\nu_e - e$ scattering.

	h_{ee} $(\times 10^{-6})$	
M_H	TEXONO	LSND
1 MeV	<4.99	<8.03
2 MeV	<0.09	<2.91
2.2 MeV	<0.02	<1.22
2.5 MeV	<0.06	<0.32
2.9 MeV	<0.02	<2.88
3 MeV	<4.58	<1.47
4 MeV	<8.45	<0.46
5 MeV	<11.46	<2.26
6 MeV	<14.27	<17.67
10 MeV	<25.02	<57.57

The differential cross sections as a function of the recoil energy T with typical reactor $\bar{\nu}_e$ spectra for the NLS1B at some specific coupling and mass parameters using the Ge detector as a target for both the FC and FV cases are displayed in Fig. 4 for illustration, where the SM contribution is superimposed. As can be seen in this figure, the cross section shows different behavior with respect to the recoil energy T, which provides more advantages in the measurements of the couplings at low energy for the low mass values of m_X. Because of the $1/T$ dependency in the cross section, working at the low-energy threshold provides better sensitivity in the coupling for small mass values of m_X. The $2m_eT$ term in the denominator can be safely neglected for high values of m_X. Therefore, the CsI(Tl) detector data are expected to provide more stringent limits since the cross section is measured at a good sensitivity in the 3–8 MeV range.

In particular, the NLS1B cross section has $1/(2m_eT+m_X^2)$ dependency, which is directly proportional to the sensitivity of the couplings of $L(R)_{e\ell'}$. When T and m_X become comparable, the $2m_eT$ term in the denominator cannot be neglected anymore. This term, however, causes us to lose the sensitivity in $\varepsilon^{L(R)}$ for low mass values of m_X. When m_X gets bigger, i.e., $m_X \gtrsim 25$ MeV, $2m_eT$ can be neglected and the sensitivity stays fixed at the minimum value as shown in Fig. 5. In this case, the $\tilde{\varepsilon}^{L(R)}_{e\ell'} = \varepsilon^{L(R)}_{e\ell'}$ and $\tilde{\varepsilon}^{V(A)}_{e\ell'} = \varepsilon^{V(A)}_{e\ell'}$ conditions are satisfied.

For the FC NLS1B interaction, the allowed regions at 90% C.L. in the parameter space of ε^{L}_{ee} and ε^{R}_{ee} with various $m_X = 1, 2, 5, 25$ MeV for TEXONO and $m_X = 3, 4, 5, 25$ MeV for LSND are illustrated in Figs. 5(a) and 5(c), respectively.

Similarly, for the FV NLS1B interaction, the allowed regions at 90% C.L. for the couplings of $\varepsilon^{L}_{e\mu(\tau)}$ and $\varepsilon^{R}_{e\mu(\tau)}$

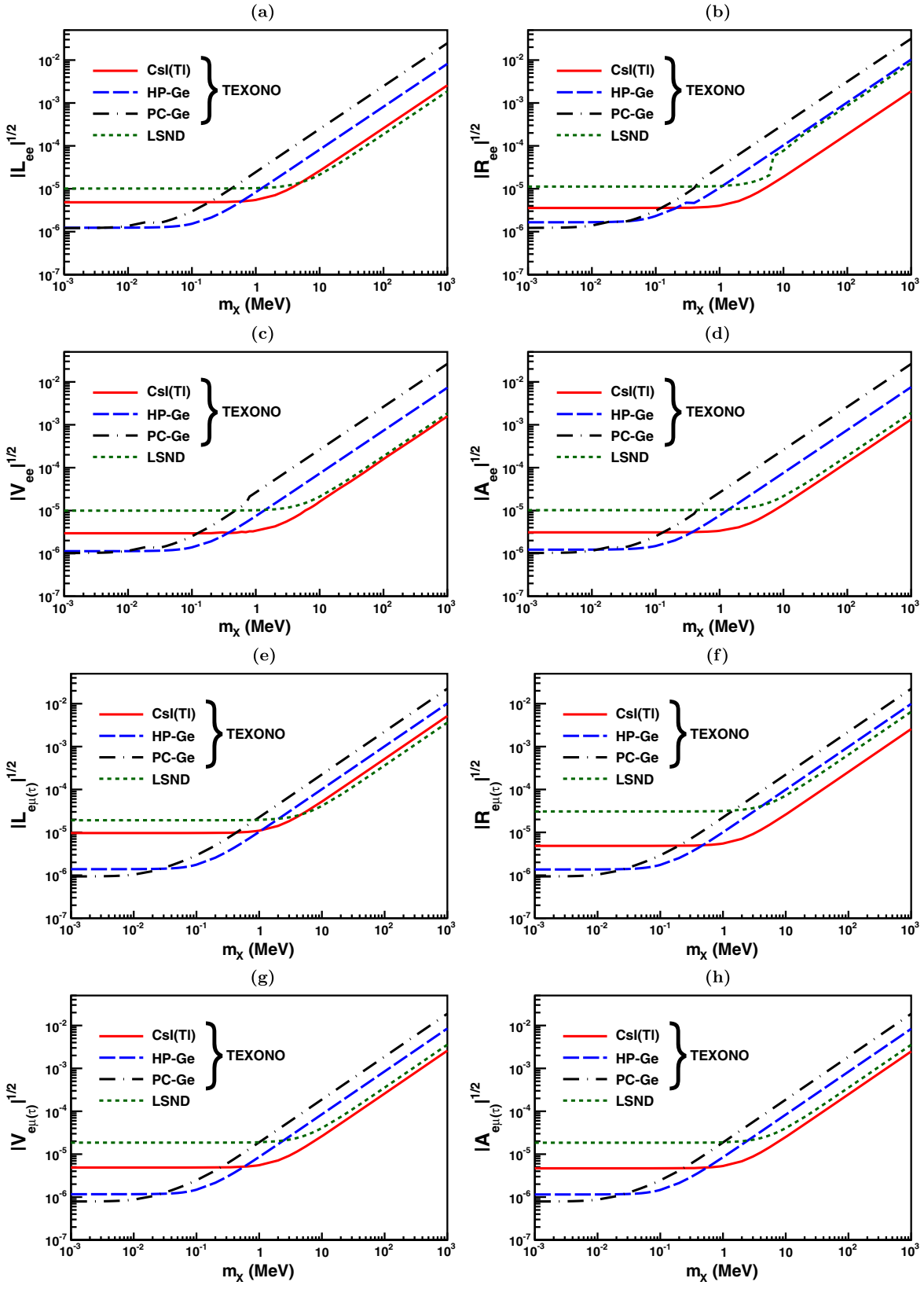

FIG. 6. The 90% C.L. upper limits for the couplings of (a) $|L_{ee}|^{1/2}$, (b) $|R_{ee}|^{1/2}$, (c) $|V_{ee}|^{1/2}$, (d) $|A_{ee}|^{1/2}$, (e) $|L_{e\mu(\tau)}|^{1/2}$, (f) $|R_{e\mu(\tau)}|^{1/2}$, (g) $|V_{e\mu(\tau)}|^{1/2}$, and (h) $|A_{e\mu(\tau)}|^{1/2}$ for TEXONO and LSND with various m_X values by adopting a one-parameter-at-a-time analysis.

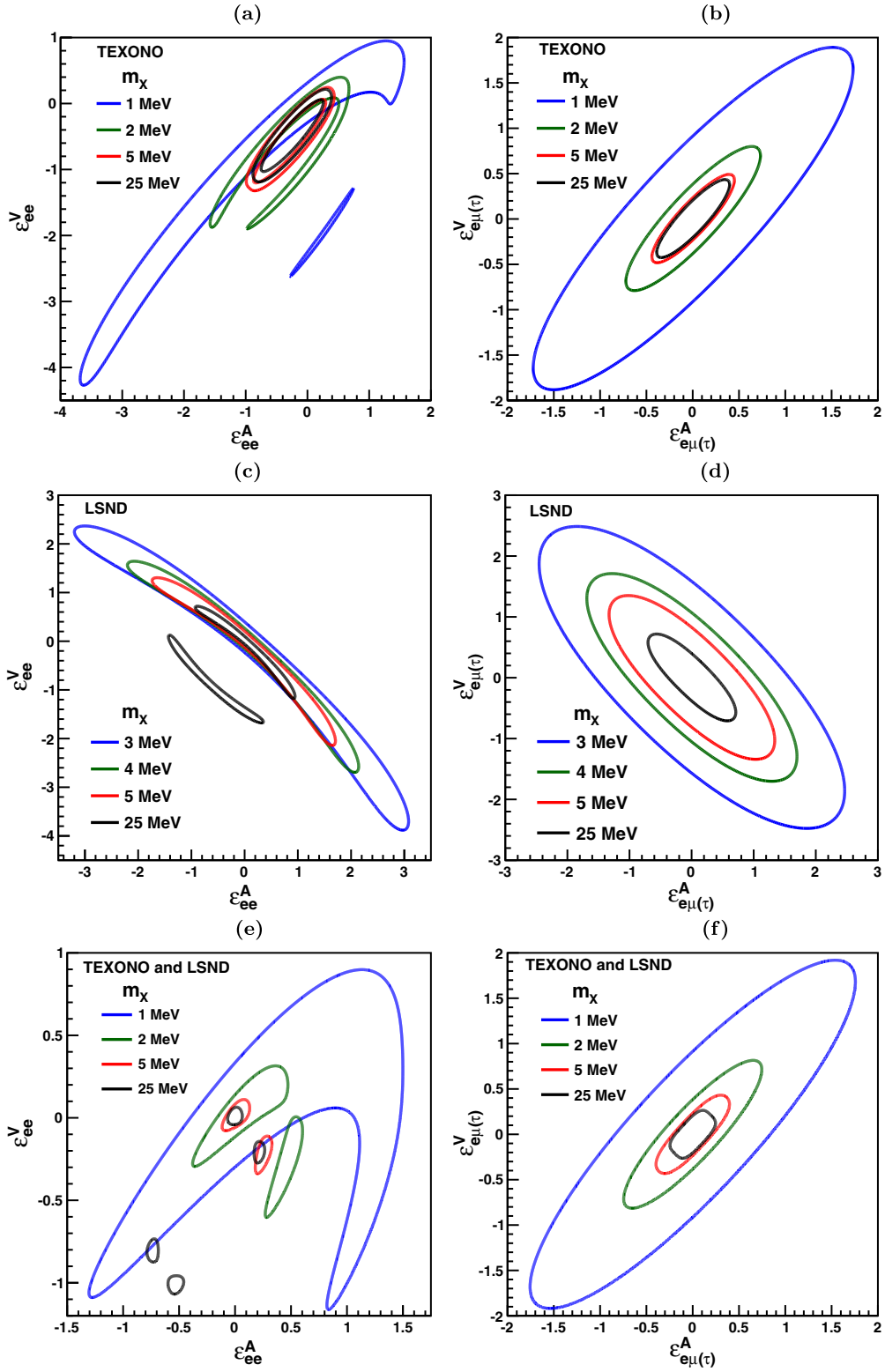

FIG. 7. The allowed regions at 90% C.L. for (a) the FC NLS1B in the parameter space of ε^V_{ee} and ε^A_{ee}; (b) FV NLS1B in the parameter space of $\varepsilon^V_{e\mu(\tau)}$ and $\varepsilon^A_{e\mu(\tau)}$ for TEXONO CsI(Tl) with various $m_X = 1, 2, 5, 25$ MeV, from outer to inner, respectively; (c) FC NLS1B in the parameter space of ε^V_{ee} and ε^A_{ee}; (d) FV NLS1B in the parameter space of $\varepsilon^V_{e\mu(\tau)}$ and $\varepsilon^A_{e\mu(\tau)}$ for LSND with various $m_X = 3, 4, 5, 25$ MeV, from outer to inner, respectively, with the global fitting for allowed regions of TEXONO CsI(Tl) and LSND at 90% C.L. for (e) FC NLS1B couplings of ε^V_{ee} vs ε^A_{ee}, and (f) FV NLS1B couplings of $\varepsilon^V_{e\mu(\tau)}$ vs $\varepsilon^A_{e\mu(\tau)}$ with various $m_X = 1, 2, 5, 25$ MeV from outer to inner, respectively.

with various $m_X = 1$, 2, 5, 25 MeV for TEXONO and $m_X = 3, 4, 5, 25$ MeV for LSND are illustrated in Figs. 5(b) and 5(d), respectively.

The global fitting for allowed regions of TEXONO and LSND for the couplings of $\varepsilon^L_{e\ell'}$ and $\varepsilon^R_{e\ell'}$ at 90% C.L. with various $m_X = 1$, 2, 5, 25 MeV are illustrated in Figs. 5(e) and 5(f) for FC and FV NSI, respectively.

By adopting a one-parameter-at-a-time analysis in the minimum χ^2 analysis, the bounds at 90% C.L. on the FC and FV NLS1B couplings for low and high mass values are given in Tables IV and V, and the upper limits at 90% C.L. are illustrated in Fig. 6 with respect to mass parameter m_X. As shown in Table IV, Table V, and Fig. 6, the TEXONO PC-Ge and HP-Ge data provide better constraints in $L(R)_{e\ell'}$ and $V(A)_{e\ell'}$ parameter spaces compared to LSND for both FC and FV NLS1B in the case of $m_X \ll 2m_eT$. On the other hand, TEXONO CsI(Tl) gives better constraints in the $L(R)_{e\ell'}$ and $V(A)_{e\ell'}$ parameter spaces compared to LSND for both FC and FV NLS1B in the case of $m_X \gg 2m_eT$.

The 90% C.L. upper limits for the couplings of $|L_{ee}|^{1/2}$, $|R_{ee}|^{1/2}$ and $|L_{e\mu(\tau)}|^{1/2}$, $|R_{e\mu(\tau)}|^{1/2}$ vs mass parameter of m_X for TEXONO and LSND are illustrated in Figs. 6(a) and 6(b) and Figs. 6(e) and 6(f), respectively. The 90% C.L. upper limits for the couplings of $|V_{ee}|^{1/2}, |A_{ee}|^{1/2}$ and $|V_{e\mu(\tau)}|^{1/2}$, $|A_{e\mu(\tau)}|^{1/2}$ versus mass parameter of m_X for TEXONO CsI(Tl) and LSND are illustrated in Figs. 6(c) and 6(d) and Figs. 6(g) and 6(h), respectively.

Similarly, the allowed regions at 90% C.L. in the parameter space of ε^V_{ee} and ε^A_{ee} with various m_X for TEXONO CsI(Tl) and LSND are illustrated in Figs. 7(a) and 7(c), respectively, for the FC NLS1B. In the case of the FV NLS1B, the allowed regions at 90% C.L. in the parameter space of $\varepsilon^V_{e\mu(\tau)}$ and $\varepsilon^A_{e\mu(\tau)}$ with various m_X for TEXONO CsI(Tl) and LSND are illustrated in Figs. 7(b) and 7(d), respectively.

The global fitting for allowed regions of TEXONO and LSND for the couplings of $\varepsilon^V_{e\ell'}$ and $\varepsilon^A_{e\ell'}$ at 90% C.L. with various $m_X = 1$, 2, 5, 25 MeV are illustrated in Figs. 7(e) and 7(f) for FC and FV NSI, respectively.

C. Charged Higgs boson

Leptons, quarks, and gauge bosons acquire their mass through the Higgs mechanism [28], while neutrinos still remain massless in the SM. In order to introduce and explain the smallness of neutrino masses without requiring an extra right-handed neutrino, one of the simplest models among other mechanisms is the Higgs triplet model (HTM), through which neutrinos gain their mass [29,30]. In HTM, apart from the neutral scalar Higgs boson (h^0), there also appear singly charged (H^+) and doubly charged (H^{++}) ones, since Higgs triplets under the standard $SU(2)_L$ gauge group have two units of weak hypercharge.

There are many phenomenological studies at high-energy accelerator experiments such as LHC and Tevatron in the literature [31,32]. However, in this study we also consider the low-energy frontier with $\bar{\nu}_e - e$ and $\nu_e - e$ elastic scattering, which are pure leptonic processes providing an elegant test to the SM of electroweak theory. The Feynman diagrams of $\bar{\nu}_e - e$ and $\nu_e - e$ scattering via the exchange of CHB are displayed in Fig. 8.

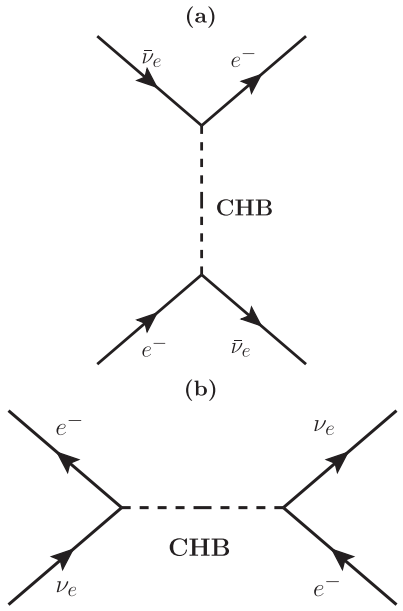

FIG. 8. Feynman diagrams of (a) $\bar{\nu}_e - e$ scattering and (b) $\nu_e - e$ scattering for the exchange of charged Higgs boson.

In the HTM, the electroweak ρ parameter is predicted at the tree level as $\rho \simeq 1\text{–}2v^2_\triangle/v^2_\Phi$, where v_Φ and $v_\triangle$ are the vacuum expectation values of the doublet Higgs field and triplet Higgs field, respectively. However, the experimental value of this parameter $\rho_{\rm exp} = 1.0004^{+0.0003}_{-0.0004}$ [33] requires that $v_\triangle$ be smaller than a few GeV, i.e., $v_\triangle < 3.5$ GeV at 95% C.L., and hence $v_\triangle/v_\Phi \lesssim 0.02$. Taking these into account, the interaction Lagrangian for the coupling of the CHB to leptons can be written as

$$\mathcal{L} = -h_{\ell\ell'}\sqrt{2}(\ell^T C P_L \nu_{\ell'} + \nu^T_\ell C P_L \ell')H^+ + \text{H.c.}, \qquad (15)$$

where $h_{\ell\ell'}$ is the coupling constant; $\ell(\ell') = $ e, μ, or τ; C is the charge conjugation; and P_L is the chiral projector.

The $\bar{\nu}_e - e$ and $\nu_e - e$ scattering differential cross sections for CHB exchange contributions are found, respectively, to be

$$\left[\frac{d\sigma_{\bar{\nu}_e e}}{dT}\right]_{\rm CHB} = \frac{m_e}{4\pi}\frac{[h^2_{ee}]^2}{[m_e(m_e+2E_\nu) - M^2_H]^2} \qquad (16)$$

and

$$\left[\frac{d\sigma_{\nu_e e}}{dT}\right]_{\rm CHB} = \frac{m_e}{4\pi}\frac{[h^2_{ee}]^2(1-T/E_\nu)^2}{[m^2_e + 2m_e(E_\nu - T) - M^2_H]^2}. \qquad (17)$$

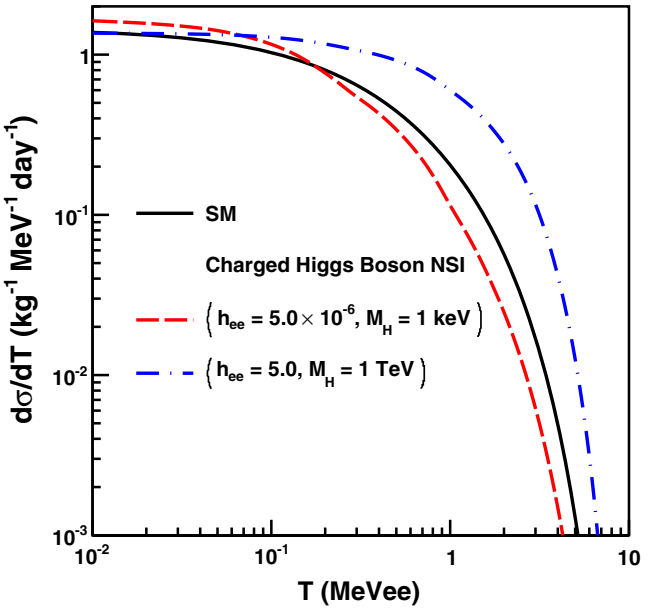

FIG. 9. Differential cross section as a function of recoil energy T with a typical reactor $\bar{\nu}_e$ spectrum for the exchange of CHB. The SM differential cross section is superimposed for comparison.

The differential cross section for CHB with relevant parameters for TEXONO CsI(Tl) is displayed in Fig. 9 with different mass parameters, where SM contribution is superimposed for comparison.

For the high mass value of CHB, the terms of $m_e(m_e + 2E_\nu)$ or $m_e^2 + 2m_e(E_\nu - T)$ in the denominator can be neglected. Therefore, $(h_{ee}/M_H)^4$ becomes a fitting parameter. From the best fit,

$$(h_{ee}/M_H)^4 = [8.32 \pm 16.74 \pm 13.39] \times 10^{-12}\ \text{GeV}^{-4} \tag{18}$$

is obtained at $\chi^2/\text{dof} = 8.8/9$ for TEXONO CsI(Tl) data. Similarly,

$$(h_{ee}/M_H)^4 = [5.21 \pm 6.10 \pm 4.51] \times 10^{-10}\ \text{GeV}^{-4} \tag{19}$$

is obtained at $\chi^2/\text{dof} = 9.7/13$ for LSND. They can be converted to their corresponding upper limit at 90% C.L. of

$$h_{ee}/M_H < 2.57 \times 10^{-3}\ \text{GeV}^{-1} \tag{20}$$

for TEXONO CsI(Tl) and

$$h_{ee}/M_H < 6.48 \times 10^{-3}\ \text{GeV}^{-1} \tag{21}$$

for LSND. TEXONO provides more stringent limits than those from LSND and a previous study given in Ref. [34] as $h_{ee}/M_H < 7.2 \times 10^{-3}\ \text{GeV}^{-1}$ for the LAMPF $\nu_e - e$ experiment [15] at 90% C.L., which was derived based on the measurement value of $\sin^2\theta_W$.

On the other hand, for the low mass value of CHB, the M_H term in the denominator can be neglected. Therefore, only $(h_{ee})^4$ becomes a fitting parameter. From the best fit,

$$(h_{ee})^4 = [1.10 \pm 4.07 \pm 3.65] \times 10^{-22} \tag{22}$$

is obtained at $\chi^2/\text{dof} = 8.8/9$ with its corresponding upper limit at 90% C.L. of

$$h_{ee} < 5.63 \times 10^{-6} \tag{23}$$

for TEXONO.

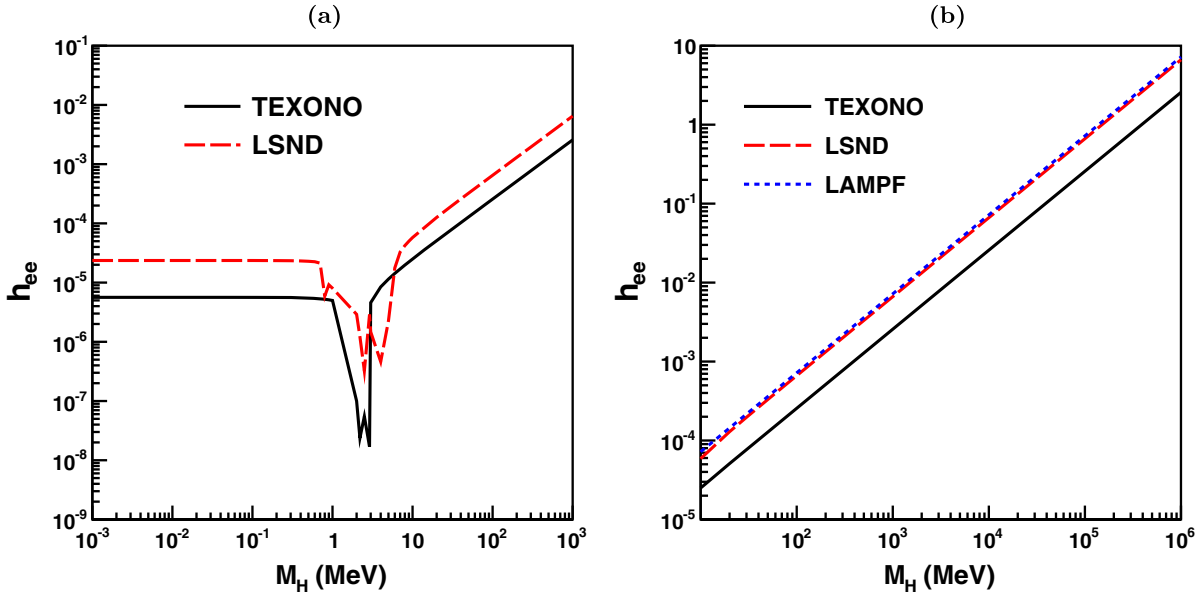

FIG. 10. The upper limit of coupling h_{ee} with respect to the mass of CHB M_H at 90% C.L. for (a) low and (b) high mass values.

Similarly, for LSND, from the best fit,

$$(h_{ee})^4 = [6.59 \pm 11.51 \pm 9.35] \times 10^{-20} \quad (24)$$

is obtained at $\chi^2/\mathrm{dof} = 10.3/13$ with its corresponding upper limit at 90% C.L. of

$$h_{ee} < 23.6 \times 10^{-6} \quad (25)$$

for the low mass value of CHB.

The upper limit of coupling h_{ee} with respect to the CHB mass values of M_H for TEXONO CsI(Tl) and LSND at 90% C.L. for low and high mass values are shown in Figs. 10(a) and 10(b), respectively. Upper bounds at 90% C.L. on the coupling of h_{ee} for $\bar{\nu}_e - e$ and $\nu_e - e$ scattering for various mass values of M_H are listed in Table VI. In this study, the parameter space is extended and consequently a new window is opened for the low mass CHB.

IV. SUMMARY AND PROSPECTS

In summary, in this article, some of the BSM new physics scenarios including massive intermediate particles such as the NLS1B, Z', and CHB have been discussed and their potential to explain some of the anomalous effects that cannot be explained by SM has been addressed.

The experimental results of upper bounds for NSI using data from the analysis of the $\bar{\nu}_e - e$ and $\nu_e - e$ elastic scattering interaction cross section measurements were placed in the framework of these BSM scenarios. The existing experimental sensitivities were improved, and the parameter space was extended by including the low-energy regime.

Particularly, in the NLS1B study, a new research window has been opened for a low mass NLS1B in the low-energy regime due to $1/T$ dependency in the cross section. For a low mass NLS1B, the coupling becomes directly proportional to $1/T$; therefore, working at low energy and low threshold becomes substantially important to see the effect of BSM. In this study we found that TEXONO gives better constraints in $\varepsilon_{ee'}^{L(R)}$ parameter space compared to the neutrino-electron channel, i.e., the LSND and LAMPF $\nu_e - e$ experiments, for both the FC and FV NLS1B cases.

In the literature, many studies on high energies have targeted high mass values of CHB. However, in this study we also considered the low-energy frontier with $\bar{\nu}_e - e$ and $\nu_e - e$ elastic scattering, which are pure leptonic processes providing an elegant test of the electroweak theory of SM. We have found new limits on the CHB couplings with respect to mass covering the low mass CHB region.

In our study of Z', the current limits were not improved since the experimental uncertainties are big compared to the heavy expectation value of the Z' mass. However, it is still interesting enough to look for the mass limits of Z' at the low-energy, low-momentum regime. This study showed that if the experimental uncertainties were improved by 1%, the current existing limits could be reached via the neutrino-electron scattering channel. By the help of the projection, it is possible to investigate the relationship between the Z' mass bounds and experimental accuracies that may provide intuitive scaling for future neutrino experiments.

ACKNOWLEDGMENTS

This work is supported by Contract No. 114F374 under the Scientific and Technological Research Council of Turkey (TÜBİTAK); Contract No. 104-2112-M-001-038-MY3 from the Ministry of Science and Technology, Taiwan; and Contract No. 2017-ECP2 from the National Center of Theoretical Sciences, Taiwan.

[1] S. F. King, J. Phys. G **42**, 123001 (2015).
[2] J. Panman, in *Precision Tests of the Standard Electroweak Model*, edited by P. Langacker (World Scientific, Singapore, 1995), pp. 504–544; W. J. Marciano and Z. Parsa, J. Phys. G **29**, 2629 (2003).
[3] T. Ohlsson, Rep. Prog. Phys. **76**, 044201 (2013).
[4] O. G. Miranda and H. Nunokawa, New J. Phys. **17**, 095002 (2015).
[5] J. Erler and P. Langacker, Phys. Lett. B **667**, 125 (2008), and references therein.
[6] M. Deniz *et al.*, Phys. Rev. D **82**, 033004 (2010); **95**, 033008 (2017).
[7] S. Bilmis *et al.*, Phys. Rev. D **85**, 073011 (2012).
[8] J.-W. Chen, H.-C. Chi, H.-B. Li, C. P. Liu, L. Singh, H. T. Wong, C.-L. Wu, and C.-P. Wu, Phys. Rev. D **90**, 011301(R) (2014).
[9] S. Bilmis, I. Turan, T. M. Aliev, M. Deniz, L. Singh, and H. T. Wong, Phys. Rev. D **92**, 033009 (2015).
[10] B. Kayser, E. Fischbach, S. P. Rosen, and H. Spivack, Phys. Rev. D **20**, 87 (1979).
[11] M. Deniz *et al.*, Phys. Rev. D **81**, 072001 (2010).
[12] H. B. Li *et al.*, Phys. Rev. Lett. **90**, 131802 (2003); H. T. Wong *et al.*, Phys. Rev. D **75**, 012001 (2007).
[13] A. K. Soma *et al.*, Nucl. Instrum. Methods Phys. Res., Sect. A **836**, 67 (2016).
[14] L. B. Auerbach *et al.*, Phys. Rev. D **63**, 112001 (2001).

[15] R. C. Allen *et al.*, Phys. Rev. D **47**, 11 (1993).
[16] G. J. Feldman and R. D. Cousins, Phys. Rev. D **57**, 3873 (1998).
[17] Y. Farzan, Phys. Lett. B **748**, 311 (2015); Y. Farzan and J. Heeck, Phys. Rev. D **94**, 053010 (2016); D. V. Forero and W. C. Huang, J. High Energy Phys. 03 (2017) 018.
[18] R. Laha, B. Dasgupta, and J. F. Beacom, Phys. Rev. D **89**, 093025 (2014).
[19] D. London and J. L. Rosner, Phys. Rev. D **34**, 1530 (1986).
[20] F. J. Petriello, S. Quackenbush, and K. M. Zurek, Phys. Rev. D **77**, 115020 (2008).
[21] J. Erler, P. Langacker, S. Munir, and E. Rojas, J. High Energy Phys. 08 (2009) 017.
[22] J. Barranco, A. Bolanos, E. A. Garces, O. G. Miranda, and T. I. Rashba, Phys. Rev. D **76**, 073008 (2007).
[23] C. Boehm, Phys. Rev. D **70**, 055007 (2004).
[24] S. N. Gninenko and N. V. Krasnikov, Phys. Lett. B **513**, 119 (2001).
[25] D. Hooper, Phys. Rev. D **75**, 123001 (2007).
[26] S. Oh and J. Tandeanb, Phys. Lett. B **697**, 41 (2011).
[27] C. W. Chiang, G. Faisel, Y. F. Lin, and J. Tandean, J. High Energy Phys. 10 (2013) 150.
[28] F. Englert and R. Brout, Phys. Rev. Lett. **13**, 321 (1964); P. W. Higgs, Phys. Rev. Lett. **13**, 508 (1964); G. S. Guralnik, C. R. Hagen, and T. W. B. Kibble, Phys. Rev. Lett. **13**, 585 (1964).
[29] T. P. Cheng and L. F. Li, Phys. Rev. D **22**, 2860 (1980); J. Schechter and J. W. F. Valle, Phys. Rev. D **22**, 2227 (1980).
[30] J. F. Ong, I. A. Jalil, and W. A. Tajuddin, Int. J. Theor. Phys. **52**, 679 (2013).
[31] P. F. Perez, T. Han, G. Huang, T. Li, and K. Wang, Phys. Rev. D **78**, 015018 (2008).
[32] A. G. Akeroyd and M. Aoki, Phys. Rev. D **72**, 035011 (2005); A. G. Akeroyd and S. Moretti, Phys. Rev. D **84**, 035028 (2011); A. G. Akeroyd and H. Sugiyama, Phys. Rev. D **84**, 035010 (2011).
[33] S. Kanemura and K. Yagyu, Phys. Rev. D **85**, 115009 (2012).
[34] J. A. Coarasa, A. Mendez, and J. Sola, Phys. Lett. B **374**, 131 (1996).